

1 INTRODUCTION

2 Above Earth's atmosphere are the Van Allen radiation belts, a toroidally-shaped  
3 pair of belts that consist of a complex and dynamic plasma environment. The inner  
4 radiation belt is stable, consists of mostly energetic protons, and is located within 2  
5 Earth radii (measured near the equator) above Earth's surface. The outer radiation  
6 belt, on the other hand, consists of mostly energetic electrons, is highly dynamic  
7 on day and hour time scales, and is typically found between 4 and 8 Earth radii  
8 above Earth's surface. These belts pose a threat to space exploration due to their  
9 adverse effects on our bodies and electrical components. A few **effects** include: a  
10 high radiation dose for manned missions, degradation of silicon that causes transistor  
11 malfunction, computer memory corruption due to bit flips, etc. With these effects in  
12 mind, it is no surprise that the radiation belts have been extensively studied since  
13 their discovery in the 1960s.

14 The radiation belt particles, mostly consisting of electrons and protons, are at  
15 times unstable to wave growth and generate electric and magnetic waves. These  
16 waves can then accelerate and scatter radiation belt particles with a variety of wave-  
17 particle mechanisms. These wave-particle interactions are believed to be responsible  
18 for scattering electron microbursts, a short and intense increase of precipitating  
19 electrons into Earth's atmosphere, that are capable of destroying ozone molecules  
20 and rapidly deplete the outer belt's electrons.

21 Electron microbursts, henceforth referred to as microbursts, are typically  
22 observed by low Earth orbiting spacecraft, sounding rockets, and high altitude  
23 balloons as a sub-second impulse of electrons. Some of the most intense microbursts  
24 have electron fluxes that are a factor of 10 to 100 above the background (for example  
25 see Fig. 7 in Blake et al. (1996)). Since they were first reported by Anderson and

26 Milton (1964), the intense transient nature of microbursts have compelled countless  
27 researchers to pursue an understanding of their properties, their effects on the  
28 environment, and the physical mechanism(s) that create microbursts. Microbursts  
29 are widely believed to be created by wave-particle scattering between a plasma wave  
30 called whistler mode chorus and outer radiation belt electrons, although many details  
31 regarding the scattering mechanism are unconstrained or unknown. The goal of this  
32 dissertation is to expand our knowledge of the wave-particle scattering mechanism  
33 that scatters electron microbursts.

34 This chapter serves as an introduction to the fundamental physical concepts  
35 that are essential to understand wave-particle interactions in Earth's magnetosphere.  
36 We will review the motion of charged particles in electric and magnetic fields, how  
37 particles are organized in the magnetosphere, how particles are accelerated and lost in  
38 the magnetosphere, and review the current state of our understanding of microbursts.

39 Then the rest of this dissertation expands our knowledge of microbursts. In  
40 Chapter ?? (chapter numbers will be filled in the full dissertation) we will investigate  
41 and model the scattering mechanism responsible for microbursts observed inside the  
42 outer radiation belt, near the magnetic equator. Then in Chapters ?? and ?? we  
43 will investigate the microburst scattering mechanism indirectly by estimating the  
44 microburst footprint size in low Earth orbit and the magnetic equator (near where  
45 microburst electrons are believed to be scattered) and compare it to sizes of chorus  
46 waves estimated in prior literature.

47 Charged Particle Motion in Electric and Magnetic Fields

A charged particle trapped in the magnetosphere will experience three types of periodic motion in Earth's nearly dipolar magnetic field in the absence of electric fields. The three motions are ultimately due to the Lorentz force that a particle of

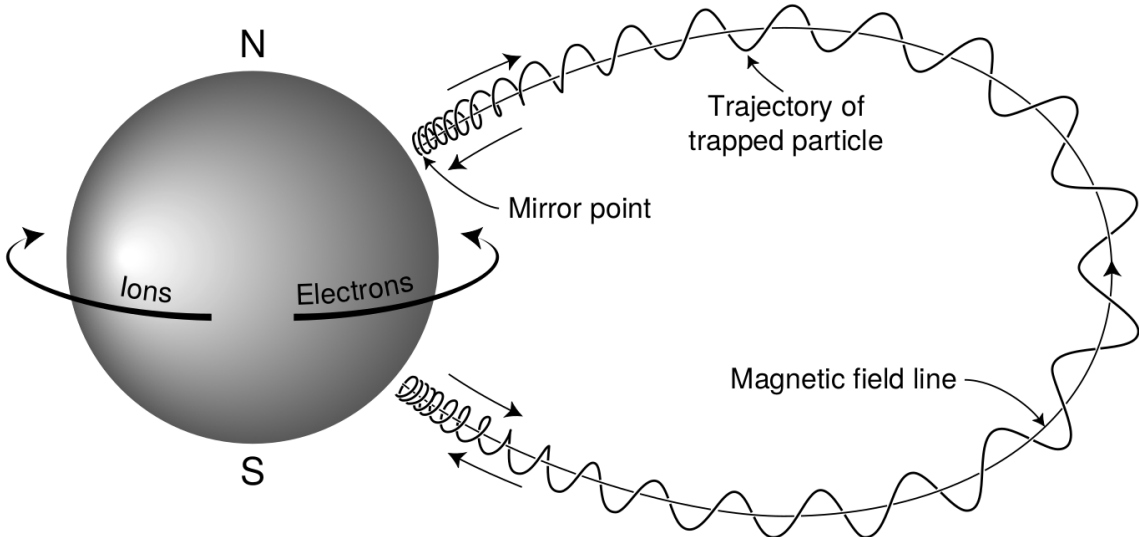


Figure 1.1: The three periodic motions of charged particles in Earth's dipole magnetic field. These motions are: gyration about the magnetic field line, bounce motion between the magnetic poles, and azimuthal drift around the Earth. Figure from (Baumjohann and Treumann, 1997).

momentum  $\vec{p}$ , charge  $q$ , and velocity  $\vec{v}$  experiences in an electric field  $\vec{E}$  and magnetic field  $\vec{B}$  and is given by

$$\frac{d\vec{p}}{dt} = q(\vec{E} + \vec{v} \times \vec{B}). \quad (1.1)$$

- <sup>48</sup> In the magnetosphere, the three periodic motions, in decreasing frequency, are
- <sup>49</sup> gyration, bounce, and drift and are schematically shown in Fig. 1.1. Each periodic
- <sup>50</sup> motion has a corresponding conserved quantity i.e. an adiabatic invariant.

The highest frequency periodic motion is gyration about a magnetic field of magnitude  $B$ . This motion is circular with a Larmor radius of

$$r = \frac{mv_{\perp}}{|q|B} \quad (1.2)$$

where  $m$  is the mass and  $v_{\perp}$  the particle's velocity perpendicular to  $\vec{B}$ . This motion

has a corresponding gyrofrequency of

$$\Omega = \frac{|q|B}{m} \quad (1.3)$$

in units of radians/second. In the radiation belts, the electron gyrofrequency,  $\Omega_e$ , is on the order of a kHz. The corresponding adiabatic invariant is found by integrating the particle's canonical momentum around the particle's path of gyration,

$$J_i = \oint (\vec{p} + q\vec{A}) \cdot d\vec{l} \quad (1.4)$$

where  $J_i$  is the  $i^{th}$  adiabatic invariant and  $\vec{A}$  is the magnetic vector potential. This integral is carried out by integrating the first term over the circumference of the gyro orbit and integrating the second term using Stokes theorem to calculate the magnetic flux enclosed by the gyro orbit. The gyration invariant is  $J_1 \sim v_\perp^2/B$  which is conserved when the frequency,  $\omega$ , of a force acting on the gyrating electron satisfies

$$\omega \ll \Omega_e.$$

The second highest frequency periodic motion is bouncing due to a parallel gradient in  $\vec{B}$ . This periodic motion naturally arises in the magnetosphere because Earth's magnetic field is stronger near the poles. To understand this motion we first we need to define the concept of pitch angle,  $\alpha$  as the angle between  $\vec{B}$  and  $\vec{v}$  which is schematically shown in Fig. 1.2a. The pitch angle relates  $v$  with  $v_\perp$  and  $v_{||}$ , the component of the particles velocity parallel to  $\vec{B}$ . As shown in Fig. 1.2b and 1.2c, a smaller (larger)  $\alpha$  will increase (decrease) the distance that the charged particle travels parallel to  $\vec{B}$  during one gyration.

Assuming the particle's kinetic energy is conserved, the conservation of  $J_1$  implies that given a particle's  $v_\perp(0)$  and  $B(0)$  at the magnetic equator (where Earth's magnetic field is usually at a minimum) we can calculate its  $v_\perp(s)$  along

the particle's path,  $s$ , by calculating  $B(s)$  from magnetic field models. Thus the particle's perpendicular velocity is then related via

$$\frac{v_{\perp}^2(0)}{B(0)} = \frac{v_{\perp}^2(s)}{B(s)} \quad (1.5)$$

<sup>65</sup> which can be rewritten as

$$\frac{v^2 \sin^2 \alpha(0)}{B(0)} = \frac{v^2 - v_{\parallel}^2(s)}{B(s)} \quad (1.6)$$

<sup>66</sup> and re-arranged to solve for  $v_{\parallel}(s)$  by

$$v_{\parallel}(s) = v \sqrt{1 - \frac{B(s)}{B(0)} \sin^2 \alpha(0)} \quad (1.7)$$

<sup>67</sup> which will tend towards 0 as the second term in the radical approaches 1.

<sup>68</sup> The location where  $v_{\parallel}(s) = 0$  is called the mirror point and is where a particle  
<sup>69</sup> reverses direction. Since Earth's magnetic field is stronger towards the poles, the  
<sup>70</sup> mirroring particle will execute periodic bounce motion between its two mirror points  
<sup>71</sup> in the northern and southern hemispheres. The corresponding adiabatic invariant,  $J_2$   
<sup>72</sup> is

$$J_2 = \oint p_{\parallel} ds \quad (1.8)$$

where  $ds$  describes the particle path between the mirror points in the northern and southern hemispheres (see Fig. 1.1).  $J_2$  is found by substituting Eq. 1.7 into Eq. 1.8 and defining the magnetic field strength at the mirror points as  $B_m$  (where  $\alpha(m) = 90^\circ$ ). The  $J_2$  integral can be written as

$$J_2 = 2p \int_{m_n}^{m_s} \sqrt{1 - \frac{B(s)}{B(m)}} ds \quad (1.9)$$

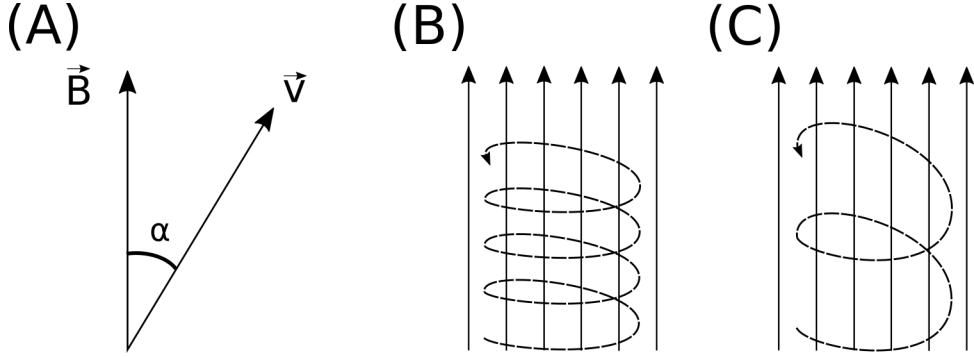


Figure 1.2: Charged particle motion in a uniform magnetic field  $\vec{B}$ . Panel (A) shows the geometry defining the pitch angle,  $\alpha$ . Panel (B) and (C) show two helical electron trajectories with dashed lines assuming a large and small  $\alpha$  (corresponding to a small and large parallel velocity  $v_{||}$ ), respectively.

73 where  $m_n$  and  $m_s$  are the northern and southern mirror points, respectively. The  
 74 bounce period can be estimated (e.g. Baumjohann and Treumann, 1997) to be

$$t_b \approx \frac{LR_e}{\sqrt{W/m}}(3.7 - 1.6 \sin \alpha(0)) \quad (1.10)$$

75 where  $W$  is the particle's kinetic energy, and  $L$  is the  $L$ -shell. The  $L$ -shell is the  
 76 distance from the Earth's center to the location where a particular magnetic field  
 77 line crosses the magnetic equator, in units of Earth radii,  $R_e$ . As with gyration, the  
 78 particle will bounce between the mirror points as long as  $\omega \ll \Omega_b$ , where  $\Omega_b$  is the  
 79 bounce frequency.

80 At this stage it is instructional to introduce loss cone pitch angle,  $\alpha_L$ .  
 81 Conventionally, the loss cone pitch angle is defined as the pitch angle where a particle  
 82 will mirror at  $\approx 100$  km altitude in the atmosphere. A charged particle gyrating at  
 83 those altitudes will encounter and Coulomb scatter with the dense atmosphere and  
 84 be lost. The 100 km altitude is only a convention and not a hard boundary, e.g. the  
 85 peak in the 1 MeV electron ionization rate is at  $\approx 60$  km altitudes (Fang et al., 2010).

86 The slowest periodic motion experienced by charged particles in Earth's

87 magnetic field is azimuthal drift around the Earth. This drift primarily results from  
 88 a combination of a radial gradient in  $\vec{B}$  and the curvature of the magnetic field. The  
 89 radial gradient drift arises because Earth's magnetic field is stronger near the Earth.  
 90 The particle's gyroradius shrinks as it gyrates towards Earth, and expands when it  
 91 gyrates away from Earth. The overall effect is the particle gyro orbit does not close  
 92 on itself causing eastward drift of negatively charged particles and westward drift  
 93 of positively charged particles. The radial gradient drift is further enhanced by the  
 94 centrifugal force that a particle experiences as it bounces along the curved field lines.  
 95 The drift adiabatic invariant,  $J_3$  is found by integrating Eq. 1.4 over the complete  
 96 particle orbit around the Earth. The shape of this drift orbit is known as a drift shell,  
 97 and can be visualized by rotating the trapped particle trajectory in Fig. 1.1 around  
 98 the axis that connects the poles. For  $J_3$ , the first term is negligible and the second  
 99 term is the magnetic flux enclosed by the drift shell,  $\Phi_m$  i.e.  $J_3 \sim \Phi_m$  Add the  $J_3$   
 100 derivation.

101 To quantify the frequencies of the three periodic motions, Fig. 1.3 from Schulz  
 102 and Lanzerotti (1974) shows contours of the gyration, bounce, and drift frequencies  
 103 for electrons and protons in Earth's dipole magnetic field.

Up until now we have considered the three periodic motions due Earth's magnetic field in the absence of electric fields. If there is an electric field,  $\vec{E}$ , perpendicular to  $\vec{B}$ , a particle's center of gyration (averaged position of the particle over a gyration) will drift with a velocity perpendicular to both  $\vec{E}$  and  $\vec{B}$ . The drift velocity can be solved using Eq. 1.1 and is

$$\vec{v}_E = \frac{\vec{E} \times \vec{B}}{B^2}. \quad (1.11)$$

104 If there is a parallel magnetic field,  $E_{||}$ , then the particle is accelerated along the  
 105 magnetic field line. An  $E_{||}$  pointing away from the Earth will contribute to the mirror

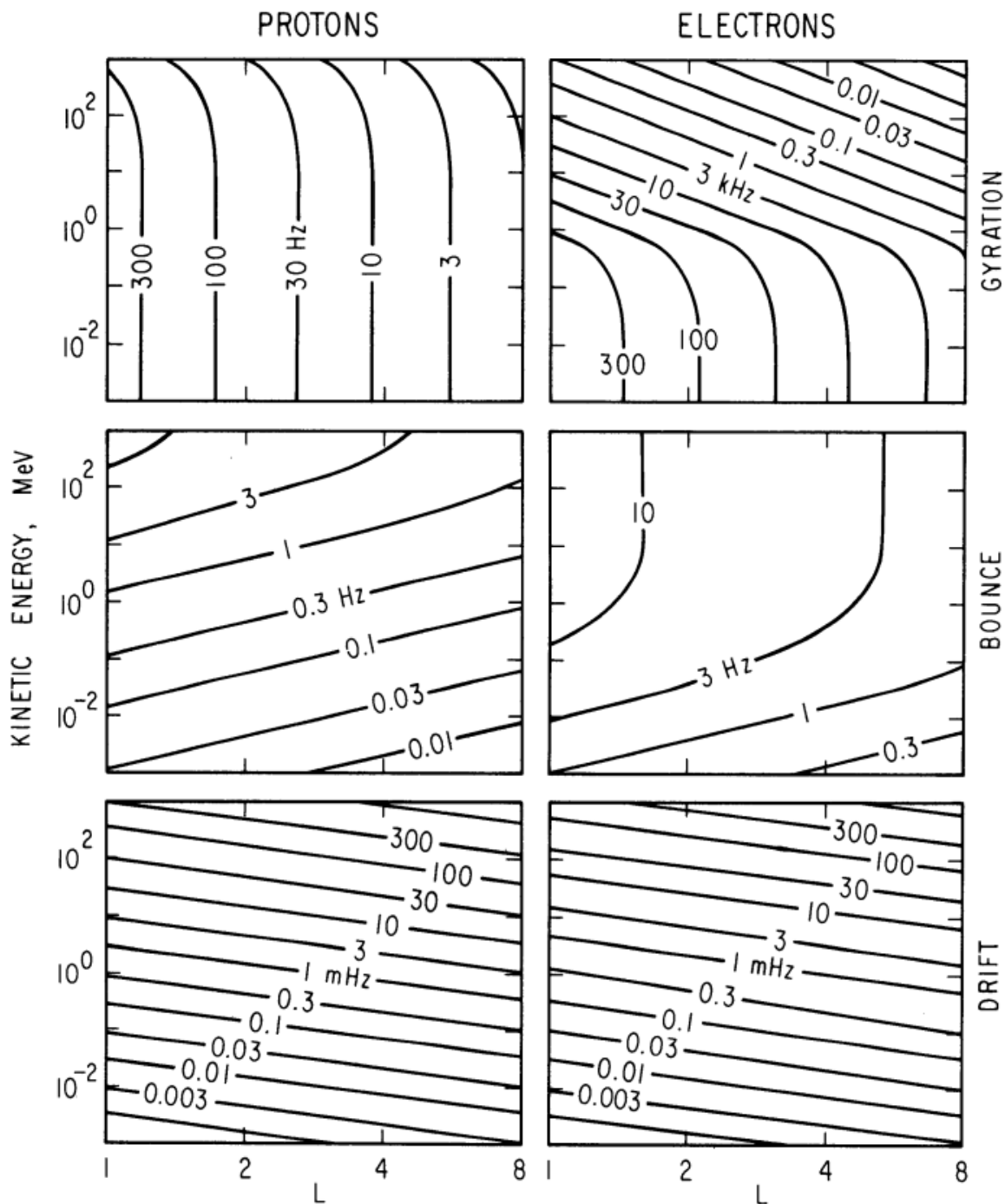


Figure 1.3: Contours of constant gyration, bounce, and drift frequencies for electrons and protons in a dipole field. Figure from Schulz and Lanzerotti (1974).

106 force and raise the particle's mirror point. On the contrary, an Earthward pointing  
 107  $E_{||}$  will oppose the mirror force and lower the mirror point. If the Earthward  $E_{||}$   
 108 lowers the mirror point into the atmosphere, those particles will precipitate into the  
 109 atmosphere. This is the mechanism that generates the aurora.

110 Particle Populations and Their Interractions in the Magnetosphere

111 Now that we have looked at the dynamics of single-particle motion in electric  
 112 and magnetic fields, we will briefly tour the various macroscopic populations in the  
 113 magnetosphere that are illustrated in Fig. 1.4.

114 The sun and its solar wind are ultimately the source of energy input into the  
 115 magnetosphere. The solar wind at Earth's orbit is a plasma traveling at supersonic  
 116 speeds with an embedded interplanetary magnetic field (IMF). When the solar wind  
 117 encounters Earth's magnetic field, the plasma can not easily penetrate into the  
 118 magnetosphere because the plasma is frozen-in on magnetic field lines. The plasma  
 119 is frozen-in on magnetic field lines because plasma has a nearly infinite conductivity.  
 120 Thus the plasma and its magnetic field drapes around the magnetosphere, forming a  
 121 cavity in the solar wind that qualitatively has a shape as shown in Fig. 1.4. The solar  
 122 wind is supersonic at 1 AU so a bow shock exists upstream of the magnetosphere  
 123 which compresses and heats the solar wind. Downstream of the bow shock, the  
 124 solar wind plasma flows around the magnetosphere inside the magnetosheath. The  
 125 magnetopause is the surface where the solar wind ram and Earth's magnetic pressures  
 126 balance. To first order, the magnetopause can be thought of as a boundary between  
 127 the solar wind and Earth's magnetosphere. The shocked plasma then flows past the  
 128 Earth where it shapes the magnetotail. In the magnetotail, the magnetopause exists  
 129 where the solar wind magnetic pressure balances Earth's magnetic field pressure in  
 130 the lobes. The magnetotail extends on the order of 100  $R_E$  downstream of Earth,

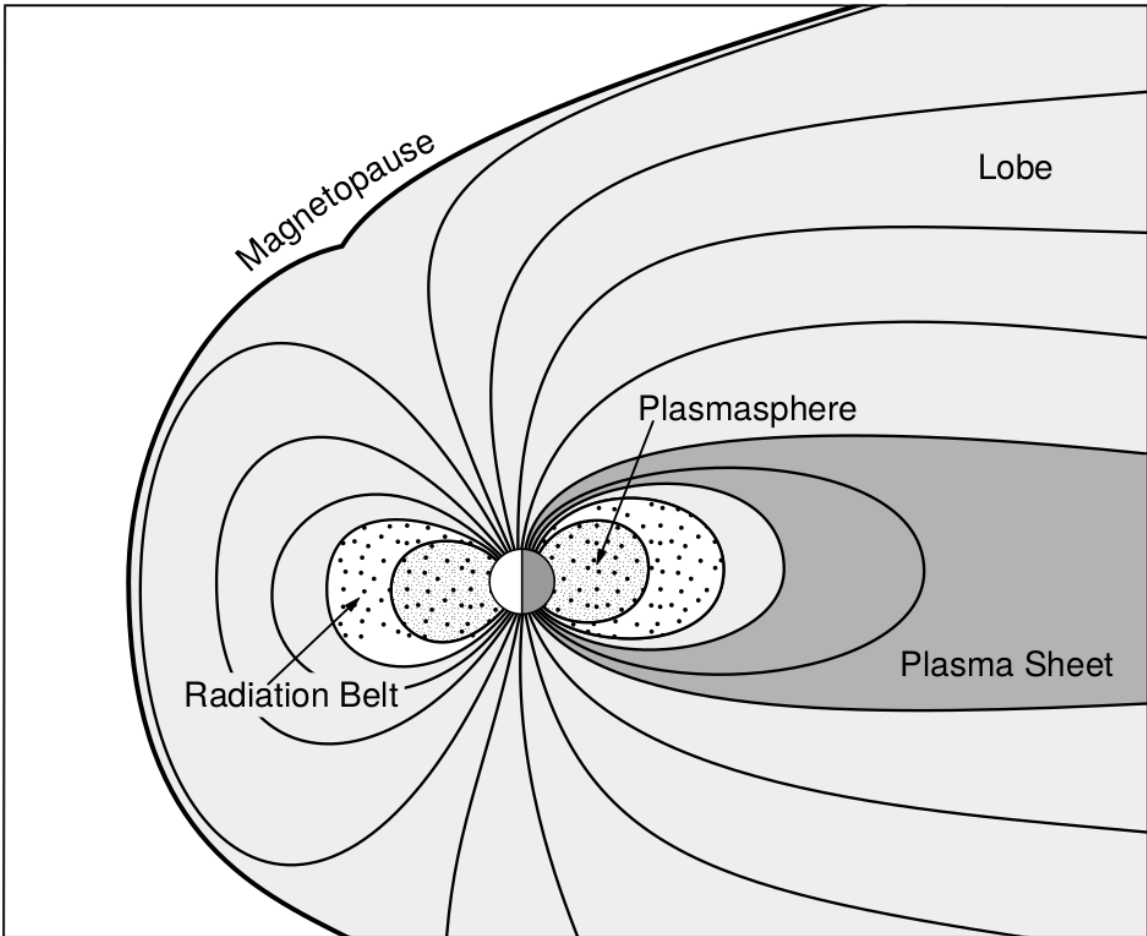


Figure 1.4: A few macroscopic structures in the magnetosphere. The magnetosphere boundary with the solar wind is the magnetopause. The magnetotail consists of two lobes that contain Earth's magnetic flux with the plasma sheet separating the two lobes. The inner magnetosphere contains the plasmasphere, the ring current, and the radiation belts which are co-located. Figure from Baumjohann and Treumann (1997).

and the tailward stretching of magnetic field lines creates a region where Earth's Earthward and anti-Earthward magnetic fields are in proximity. In this region, the curl of  $\vec{B}$  is non-zero, thus by Ampere's law there must be a current (called the plasma sheet) near the magnetic equator (e.g. Eastwood et al., 2015).

### Populations in the Inner Magnetosphere

Closer to Earth, where the magnetic field is largely dipolar, are three plasma populations that comprise the inner magnetosphere: the plasmasphere, the ring current, and the radiation belts which are shown in Fig. 1.4. Before we describe these three particle populations in detail, we will introduce the coordinate system that most naturally describes the inner magnetosphere environment, and the electric fields that mostly effect low energy particles.

In this coordinate system the “radial” coordinate was defined in section 1 and is the L shell. The azimuthal coordinate is the magnetic local time (MLT). For an observer above Earth's north pole looking down, MLT is defined to be 0 (midnight) in the anti-sunward direction and increases in the counter-clockwise direction with 6 at dawn, 12 at noon (sunward direction), and 18 in dusk. The final coordinate is the magnetic latitude,  $\lambda$ , which is analogous to the latitude coordinate in the spherical coordinate system and is defined to be 0 at the magnetic equator. This coordinate system is shown in Fig. 1.5 and naturally describes the inner magnetosphere populations described below.

The low energy particle dynamics in the inner magnetosphere are organized by the co-rotation and the dawn-dusk (pointing from approximately 6 to 18 MLT) electric fields. The co-rotation electric field arises from Earth's rotation. Earth's magnetic field and the particles frozen on it rotate with the Earth so in the magnetosphere (non-rotating) reference frame the particles appear to  $\vec{E} \times \vec{B}$  drift with Earth's

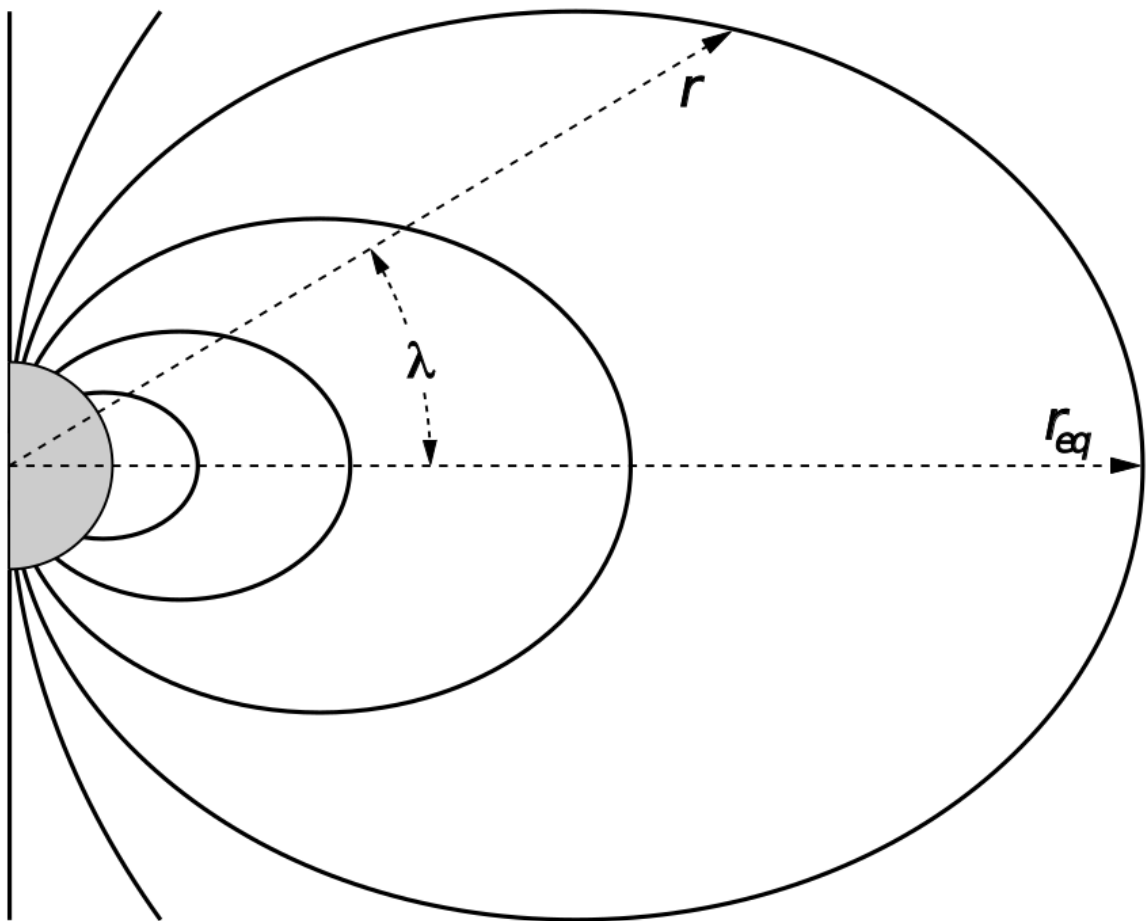


Figure 1.5: The dipole coordinate system. The magnetic latitude of  $\mathbf{r}$  is  $\lambda$ . The radial distance to a magnetic field line in the equatorial plane is typically given by  $L = r_{eq}/R_e$ . Figure from Baumjohann and Treumann (1997).

156 rotation. Make sure the E cross B drift is references correctly. Thus the co-rotation  
 157  $\vec{E}$  points towards Earth. The other electric field points from dawn to dusk is called  
 158 the convection electric field and is due to the Earthward transport of particles from  
 159 the magnetotail. In the magnetosphere reference frame this motion appears as an  
 160 electric field pointing from dawn to dusk. The superposition of the co-rotation and  
 161 and convection electric fields is a potential field shown in Fig. 1.6. The shaded  
 162 area in Fig. 1.6 shows where low energy electrons execute closed orbits around Earth  
 163 (i.e. particles are trapped), and outside this region the particles are not trapped. The  
 164 dynamic topology of the shaded region in Fig. 1.6 is controlled by only the convection  
 165 electric field which is dependent on the solar wind speed and the IMF. Due to  $\vec{E} \times \vec{B}$   
 166 drift, the lowest energy particles orbit along equipotential lines in the shaded region  
 167 in Fig. 1.6 and make up the plasmasphere.

168 Plasmasphere The plasmasphere is a relatively dense ( $n_e \sim 10^3/\text{cm}^3$ ) and cool  
 169 ( $\sim \text{eV}$ ) plasma. The plasmasphere typically extends to  $L \sim 4$  and the spatial extent  
 170 is highly dependent on the solar wind and magnetospheric conditions. The source  
 171 of the plasmasphere is the ionosphere, a layer in Earth's upper atmosphere that  
 172 contains a high concentration of electrons and ions. The main mechanisms that  
 173 ionize the ionosphere are ultraviolet light from the sun and particle precipitation.  
 174 The ultraviolet ionization by sunlight is strongly dependent on the time of day  
 175 and latitude, while particle precipitation is highly dependent on magnetospheric  
 176 conditions and mostly occurs at high latitudes.

177 The outer boundary of the plasmasphere is called the plasmapause which is  
 178 typically identified by a steep radial gradient in plasma density from  $\sim 10^3/\text{cm}^3$  to  
 179  $\sim 1/\text{cm}^3$ . It is important to know the location of the plasmapause since the plasma  
 180 density strongly controls the efficiency of particle scattering by waves. For example,

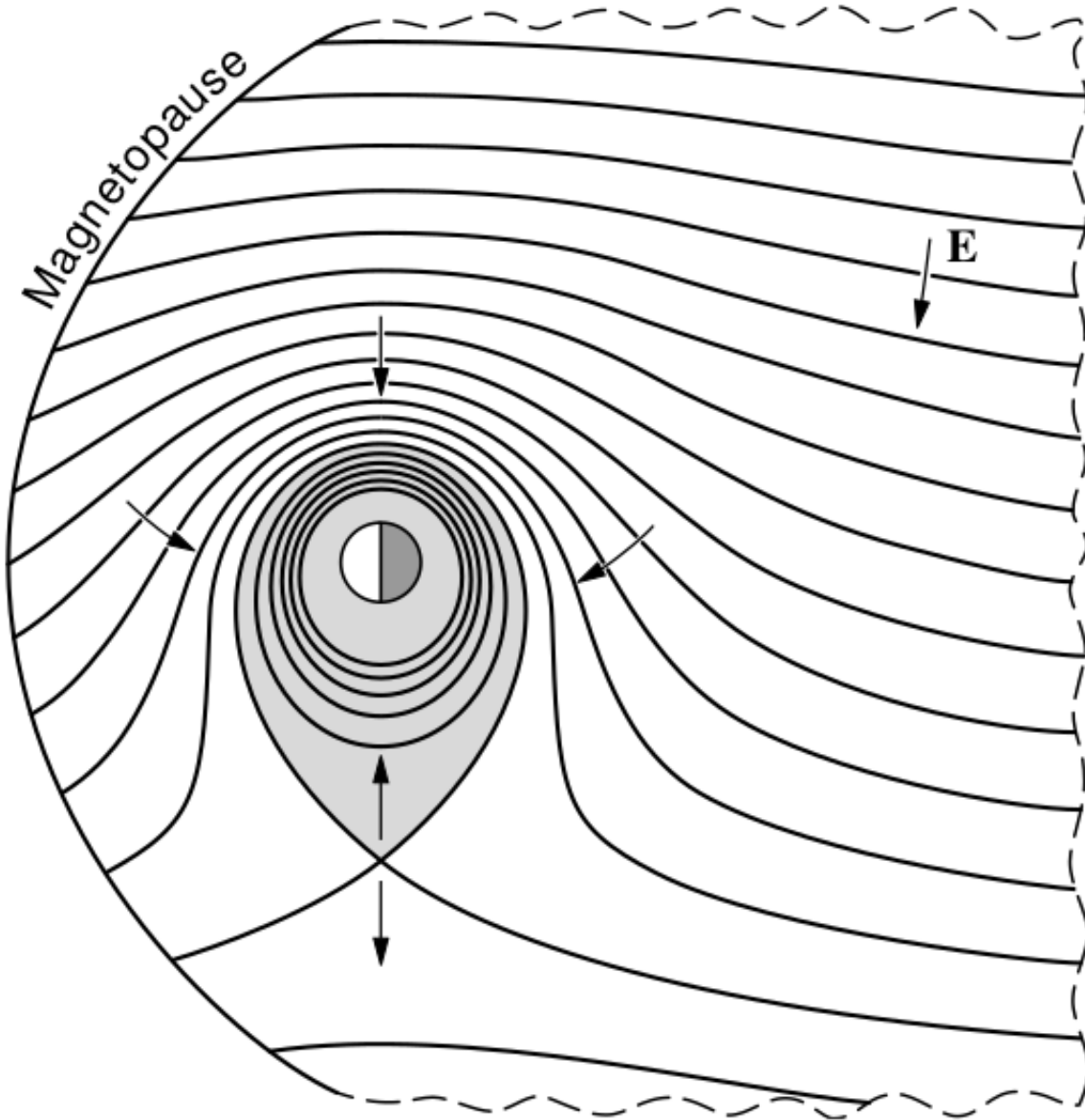


Figure 1.6: Equipotential lines and electric field arrows due to the superposition of the co-rotation and convection electric fields. Electrons in the shaded region execute closed orbits. Outside of the shaded regions the electrons are not trapped and will escape. The region separating the two regimes is called the Alfvén layer. Figure from Baumjohann and Treumann (1997).

181 electron scattering by chorus waves is more efficient when the ratio of the plasma and  
 182 gyro frequency is low which is typically found in low plasma density regions outside  
 183 of the plasmapause (e.g. Horne et al., 2003, 2005; O'Brien and Moldwin, 2003).

184 Ring Current A higher energy population is the ring current. This population  
 185 consists of protons and electrons between tens and a few hundred keV that drift  
 186 around the Earth. The orbits of higher energy particles are not as affected by the  
 187 convection and co-rotation electric field, instead they drift around the Earth due to  
 188 gradient and curvature drifts. Since the direction of the drift is dependent on charge,  
 189 protons drift west around the Earth and electrons drift East. This effect creates a  
 190 current around the Earth.

191 The ring current generates a magnetic field which decreases the magnetic field  
 192 strength at the surface of the Earth and increases it outside of the ring current.  
 193 The decrease of Earth's magnetic field strength is readily observed by a system of  
 194 ground-based magnetometers and is merged into a Disturbance Storm Time (DST)  
 195 index to quantify the global reduction in the magnetic field. An example of a DST  
 196 index time series from the 2015 St. Patrick's Day storm, driven by a coronal mass  
 197 ejection (CME), is shown in Fig. 1.7. A few notable features of the storm and the  
 198 ring current are worth mentioning. At the start of the storm the ring current is  
 199 sometimes depleted and DST increases slightly (termed the initial phase or sudden  
 200 storm commencement) and is shown by the red horizontal bar in Fig. 1.7. During  
 201 the main phase of the storm the ring current population is rapidly built up and DST  
 202 rapidly decreases which is shown by the green bar in Fig. 1.7. After the storm passes,  
 203 the ring current gradually decays toward its equilibrium state over a period of a few  
 204 days and DST returns towards zero during the recovery phase which is shown by the  
 205 blue bar in Fig. 1.7. The DST index, along with other geomagnetic indices, are used

206 by the space physics community to quantify the global state of the magnetosphere.

207 Radiation Belts The highest particle energy populations are in the Van Allen  
208 radiation belts. These belts were discovered by Van Allen (1959) and Vernov and  
209 Chudakov (1960) during the Cold War and are a pair of toroidally shaped populations  
210 of trapped electrons and protons shown in Fig. 1.8. Their quiescent toroidal shape,  
211 similar to the shape of the plasmasphere and ring current, is a result of Earth's dipole  
212 magnetic field.

213 The inner radiation belt is extremely stable on time periods of years, extends  
214 to  $L \approx 2$ , and mainly consists of protons with energies between MeV and GeV and  
215 electrons with energies up to  $\approx 1$  MeV (Claudepierre et al., 2019). The source of  
216 inner radiation belt protons is believed to be due to cosmic-ray albedo neutron decay  
217 (e.g. Li et al., 2017) and inward radial diffusion for electrons (e.g. O'Brien et al.,  
218 2016). The gap between the inner and outer radiation belt is called the slot, which is  
219 believed to be due to hiss waves inside the plasmasphere (described below) scattering  
220 particles into the atmosphere (e.g. Breneman et al., 2015; Lyons and Thorne, 1973).

221 The outer radiation belt is much more dynamic and consists of mainly electrons  
222 of energies up to a few MeV. The outer belt's spatial extent is highly variable as  
223 shown in Fig. 1.9, and is typically observed between L of 4 and 8. The source of  
224 outer radiation belt electrons is widely believed to be injections of plasma from the  
225 magnetotail that is then accelerated to high energies.

226 Due to the highly energetic and dynamic nature of the radiation belts, and  
227 their impact on space exploration, the radiation belts have been studied for over half  
228 century. Researchers have studied and attempted to predict the dynamics of radiation  
229 belt particles, waves, and wave-particle interactions by considering various competing  
230 particle acceleration and loss mechanisms which are described next.

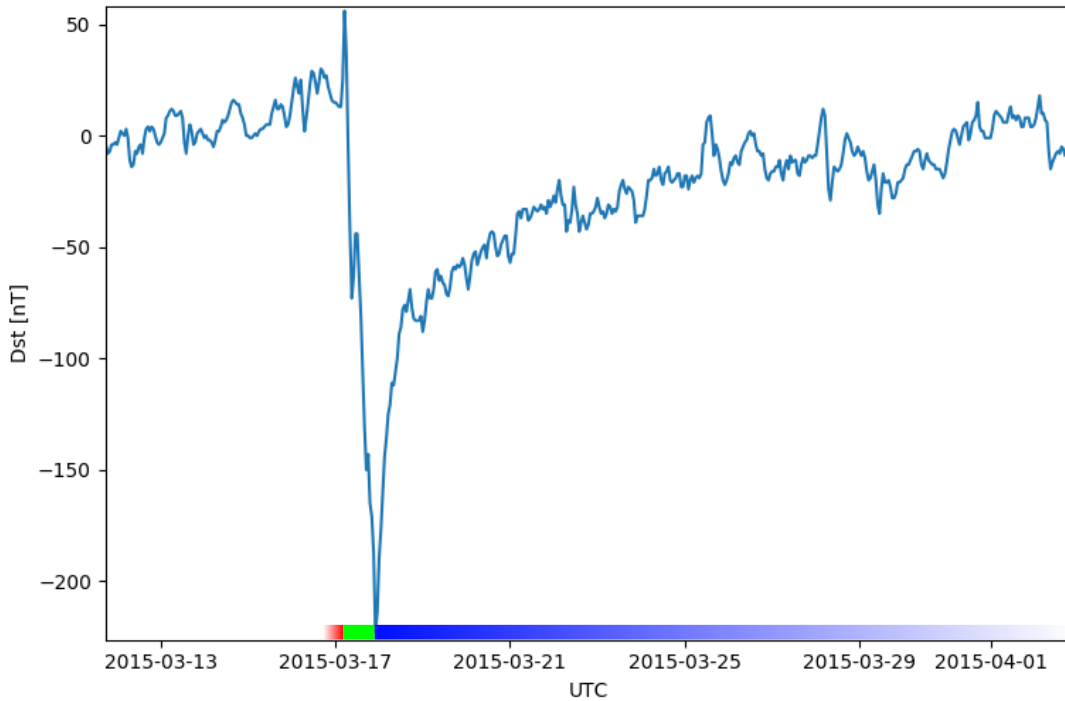


Figure 1.7: The DST index during the St. Patrick's Day 2015 storm. This storm was caused by a coronal mass ejection on March 15th, 2015. The storm phases are: initial phase, main phase, and recovery phase. The initial phase occurred when the Dst peaked at +50 nT on March 17th during which the ring current was eroded by the coronal mass ejection during the interval shown by the red bar shown at the bottom. Then the following rapid decrease to  $\approx -200$  nT was during the main phase where many injections from the magnetotail enhanced the ring current, which reduced Earth's magnetic field strength at the ground, and is shown with the green bar. Lastly, the recovery phase lasted from March 18th to approximately March 29th during which the ring current particles were lost and the ring current returned to its equilibrium state. The recovery phase is shown with the blue bar.

## The Earth's Electron Radiation Belts

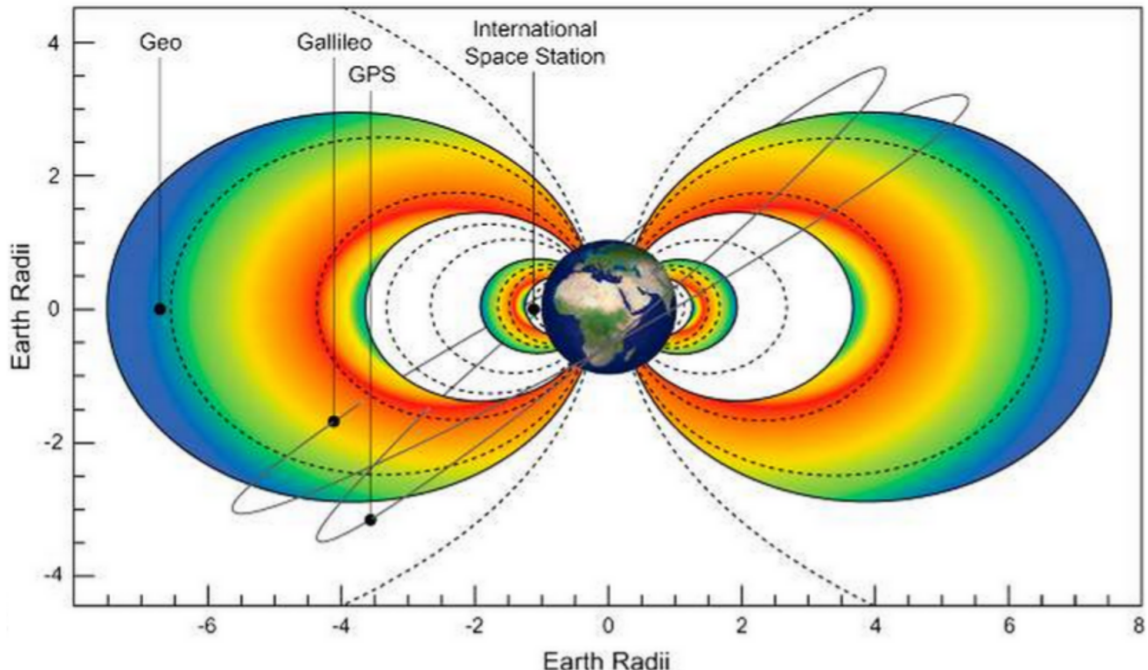


Figure 1.8: The two radiation belts with the locations of various satellites and orbits. Figure from (Horne et al., 2013).

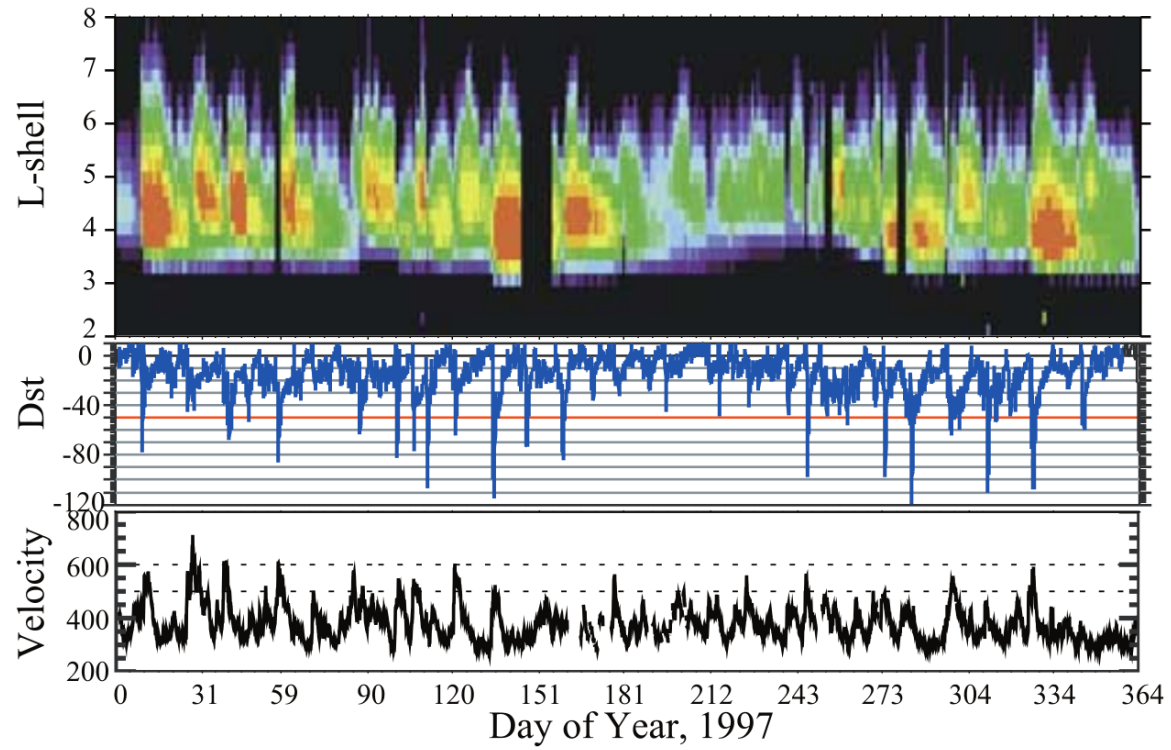


Figure 1.9: The dynamics of the outer radiation belt in 1997 from the POLAR satellite. Top panel shows the 1.2-2.4 MeV electron flux as a function of L and 1997 day of year. The middle panel shows the DST index, and bottom panel shows the solar wind velocity. Figure from (Reeves et al., 2003).

231

Radiation Belt Particle Sources and Sinks

232 In the magnetosphere there are a variety of mechanisms that add and remove  
 233 particles. In the radiation belts, there is a complex interplay between these  
 234 mechanisms that cause substantial changes to the radiation belt particle fluxes. An  
 235 example of the complex radiation belt dynamics from 1997 is shown in the top panel  
 236 in Fig. 1.9. This section will introduce a few mechanisms that contribute to the  
 237 highly dynamic radiation belt fluxes including: adiabatic heating, wave-resonance  
 238 heating, magnetopause shadowing, and wave-particle scattering.

239 Adiabatic Heating

240 One of the particle heating and transport mechanisms arises from the Earthward  
 241 convection of particles. As shown in Eq. 1.5, the conservation of  $J_1$  implies that the  
 242 initial and final  $v_\perp$  depends on the change in the magnetic field magnitude. As a  
 243 particle convects Earthward  $B_f > B_i$  and thus  $v_\perp$  must also increase. The dipole  
 244 magnetic field magnitude in micro Tesla ( $\mu T$ ) can be written as

$$B(L, \lambda) = \frac{31.2 \text{ } \mu\text{T}}{L^3} \sqrt{1 + 3 \sin^2 \lambda} \quad (1.12)$$

245 The change in  $v_\perp^2$  can be found by taking the ratio of  $B(L, \lambda)$  at two different  $L$  shells

$$\frac{v_{\perp f}^2}{v_{\perp i}^2} = \left( \frac{L_i}{L_f} \right)^3 \quad (1.13)$$

246 thus the increase in  $v_\perp \sim (L_i/L_f)^{3/2}$ .

247 As the particle convects Earthward its  $v_{||}$  also increases because the distance  
 248 between the particle's mirror points decrease. Calculating the increase in  $v_{||}$  is

<sup>249</sup> somewhat difficult, but if  $J_2$  is conserved the increase in  $v_{\parallel}$  is approximately

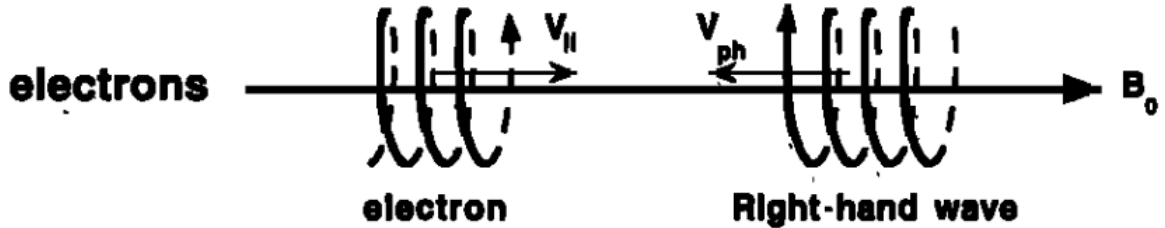
$$\frac{v_{\parallel f}^2}{v_{\parallel i}^2} = \left( \frac{L_i}{L_f} \right)^k \quad (1.14)$$

<sup>250</sup> where  $k$  ranges from 2 for equatorial pitch angles,  $\alpha_{eq} = 0^\circ$ , to 2.5 for  $\alpha_{eq} = 90^\circ$   
<sup>251</sup> (Baumjohann and Treumann, 1997). Since the rate of adiabatic heating is greater in  
<sup>252</sup> the perpendicular direction than heating in the parallel direction, an initially isotropic  
<sup>253</sup> particle distribution will become anisotropic during its convection. These isotropic  
<sup>254</sup> particles can then become unstable to wave growth and generate waves in order to  
<sup>255</sup> reach equilibrium.

<sup>256</sup> Wave Resonance Heating

<sup>257</sup> Another mechanism that heats particles is caused by particles resonating with  
<sup>258</sup> plasma waves. A few of the electromagnetic wave modes responsible for particle  
<sup>259</sup> acceleration (and scattering) relevant to radiation belt dynamics are hiss, whistler  
<sup>260</sup> mode chorus (chorus), and electromagnetic ion cyclotron (EMIC) waves. These waves  
<sup>261</sup> are created by the loss cone instability that is driven by an anisotropy of electrons for  
<sup>262</sup> chorus waves, and protons for EMIC waves. The level of anisotropy can be quantified  
<sup>263</sup> by the ratio of the perpendicular to parallel particle temperatures ( $T_{\perp}/T_{\parallel}$ ). A particle  
<sup>264</sup> distribution is unstable when  $T_{\perp}/T_{\parallel} > 1$ . Since electrons gyrate in a right-handed  
<sup>265</sup> sense, the chorus waves also tend to be right hand circularly polarized (Tsurutani and  
<sup>266</sup> Lakhina, 1997). The same argument also applies to protons and left hand circularly  
<sup>267</sup> polarized EMIC waves.

<sup>268</sup> These circularly polarized waves can resonate with electrons and/or protons  
<sup>269</sup> when their relative motion results in a static  $\vec{E}$  in the particle's reference frame. One  
<sup>270</sup> example of a resonance between a right hand circularly polarized wave and an electron  
<sup>271</sup> is shown in Fig. 1.10. The electron's  $v_{\parallel}$  and the wave's parallel wave vector,  $k_{\parallel}$ , are in



$$\omega + k_{\parallel}v_{\parallel} = \Omega^-$$

Figure 1.10: The trajectories of an electron and a right-hand circularly polarized wave during a cyclotron resonance. The electron's  $v_{\parallel}$  and the wave's  $k_{\parallel}$  are in opposite directions such that the wave's frequency is Doppler shifted to an integer multiple of the electron cyclotron frequency. Figure from (Tsurutani and Lakhina, 1997).

<sup>272</sup> opposite directions such that the wave frequency,  $\omega$ , is Doppler shifted to an integer  
<sup>273</sup> multiple of the  $\Omega_e$  where the electron feels a static electric field and is accelerated or  
<sup>274</sup> decelerated. Quantitatively, this resonance condition is easier to understand with the  
<sup>275</sup> following toy model.

<sup>276</sup> Assume a uniform magnetic field,  $\vec{B} = B_0\hat{z}$ , with a parallel propagating ( $k = k\hat{z}$ ),  
<sup>277</sup> right-hand circularly polarized wave. The wave's electric field as a function of position  
<sup>278</sup> and time can be written as

$$\vec{E} = E_0(\cos(\omega t - kz)\hat{x} + \sin(\omega t - kz)\hat{y}). \quad (1.15)$$

The angular component of  $\vec{E}$  that will effect the particle's  $v_{\perp}$  is

$$E_{\theta} = \vec{E} \cdot \hat{\theta} = E_0 \cos(\omega t - kz + \theta). \quad (1.16)$$

<sup>279</sup> Now assume that the electron is traveling in the  $-\hat{z}$  direction with a velocity,  $\vec{v} =$

<sup>280</sup>  $-v_0\hat{z}$ , so its time dependent position along  $\hat{z}$  is

$$z(t) = -v_0 t \quad (1.17)$$

<sup>281</sup> and gyrophase is

$$\theta(t) = -\Omega t + \theta(0) \quad (1.18)$$

<sup>282</sup> where the first negative sign comes from the electron's negative charge. Now we put  
<sup>283</sup> this all together into Eq. 1.1 and find the force that the electron will experience is

$$m \frac{dv_\theta}{dt} = qE_\theta = qE_0 \sin((\omega + kv_0 - \Omega)t + \theta(0)). \quad (1.19)$$

<sup>284</sup> This is a relatively complex expression, but when the time dependent component is  
<sup>285</sup> zero, i.e.

$$\omega + kv_0 - \Omega = 0, \quad (1.20)$$

<sup>286</sup> the electron will feel a static electric field and be accelerated or decelerated depending  
<sup>287</sup> on  $\theta_0$ , the phase between the wave and the electron. The expression in Eq. 1.20 is  
<sup>288</sup> commonly referred to as the resonance condition and is more generally written as

$$\omega - k_{||}v_{||} = \frac{n\Omega_e}{\gamma} \quad (1.21)$$

<sup>289</sup> where  $n$  is the resonance order, and  $\gamma$  is the relativistic correction (e.g. Millan and  
<sup>290</sup> Thorne, 2007). In the case of the cyclotron resonance ( $n = 1$ ), the wave and cyclotron  
<sup>291</sup> frequencies are approximately equal and thus  $J_1$  is violated. Since  $J_1$  is violated,  $J_2$   
<sup>292</sup> and  $J_3$  are also violated since the conditions required to violate  $J_2$  and  $J_3$  are less  
<sup>293</sup> stringent than  $J_1$ . It is important to remember that a particle will experience the

294 effects of many waves along its drift orbit. The typical MLT extent of a handful of  
 295 waves that are capable of resonating with radiation belt electrons are shown in Fig.  
 296 1.11.

297 Particle Losses

298 Now that we have seen two general mechanisms with which particles are  
 299 accelerated in the magnetosphere, we will consider a few specific mechanisms that  
 300 remove particles from the magnetosphere into the atmosphere or the solar wind.  
 301 One mechanism that transports magnetosperic particles into the solar wind is  
 302 magnetopause shadowing (e.g. Ukhorskiy et al., 2006). Magnetopause shadowing  
 303 occurs when the ring current is strengthened and Earth's magnetic field strength is  
 304 increased outside of the ring current. If the ring current increases slowly enough (such  
 305 that  $J_3$  is conserved), a particle drift shell will move outward to conserve  $J_3$ . If the  
 306 particle's drift shell expands past the magnetopause, the particle will be lost to the  
 307 solar wind.

308 Another particle loss (and acceleration) mechanism is called radial diffusion and  
 309 is driven by ultra low frequency (ULF) waves. Radial diffusion is the transport of  
 310 particles from high to low phase space density,  $f$ . If the transport is radially inward,  
 311 particles will appear to be accelerated. On the other hand, radially outward radial  
 312 diffusion can transport particles through the magnetopause where they will be lost  
 313 to the solar wind. Reeves et al. (2013) investigated the driver of particle acceleration  
 314 during the October 2012 storm and observationally found that inward radial diffusion  
 315 was not dominant, rather local acceleration via wave-resonance heating appeared to  
 316 be the dominant acceleration mechanism.

317 The loss mechanism central to this dissertation is pitch angle and energy  
 318 scattering of electrons by waves. Some of the waves that scatter electrons in energy

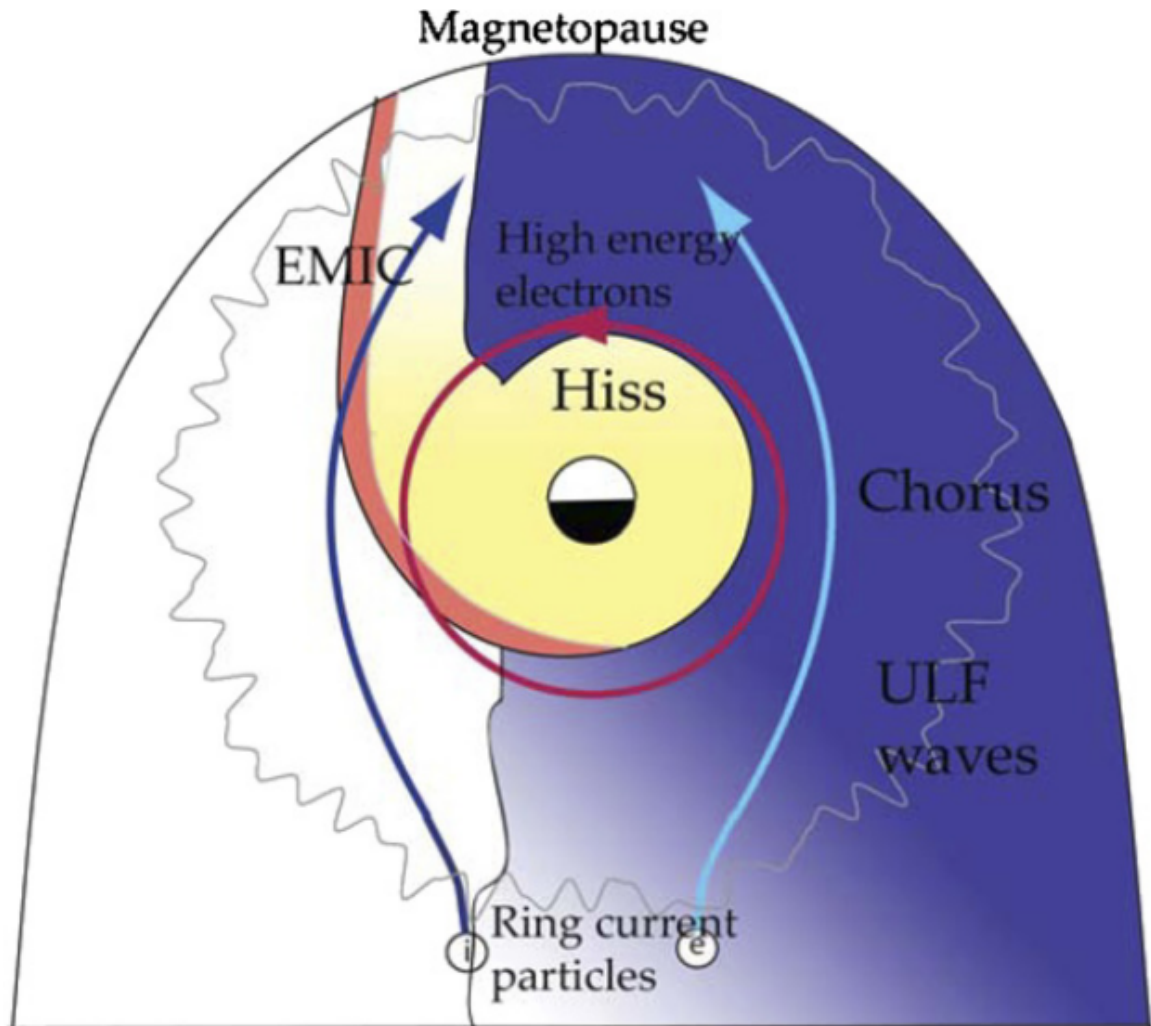


Figure 1.11: Various wave modes in the magnetosphere. Ultra low frequency waves occur through the magnetosphere. Chorus waves are typically observed in the 0-12 midnight-dawn region. EMIC waves are typically observed in the dusk MLT sector. Hiss waves are observed inside the plasmasphere. Figure from Millan and Thorne (2007).

and pitch angle in the inner magnetosphere are: plasmaspheric hiss (e.g. Breneman et al., 2015; O'Brien et al., 2014), EMIC waves (e.g. Capannolo et al., 2019; Hendry et al., 2017), and chorus waves (e.g. Breneman et al., 2017; Kasahara et al., 2018; Ozaki et al., 2019). These wave-particle interactions occur when the resonance condition in Eq. 1.21 is satisfied and the particle's energy and  $\alpha$  is modified by the wave. More details regarding the theory of pitch angle and energy diffusion is given in Chapter ???. If the wave changes  $\alpha$  towards zero and  $\alpha < \alpha_L$ , then the particle's mirror point dips below 100 km altitude where the particle can be lost from the magnetosphere. One manifestation of pitch angle scattering of particles into the loss cone are microbursts, a sub-second duration impulse of electrons.

329

### Microbursts

Microbursts were first seen with high altitude balloons which measured bremsstrahlung X-rays emitted by microburst electrons impacting the atmosphere by Anderson and Milton (1964). In the following years, numerous balloon flights expanded our knowledge of non-relativistic ( $< 500$  keV) microbursts by quantifying the microburst spatial extent, temporal width, occurrence frequency, extent in L and MLT, and their source. It is worth noting that relativistic microbursts have not yet been observed by high altitude balloons. The microburst source was initially believed to be either a local plasma instability or a propagating disturbance in the magnetosphere (Barcus et al., 1966; Brown et al., 1965; Parks, 1967; Trefall et al., 1966). Soon after, both non-relativistic and relativistic microbursts electrons were directly observed in LEO with spacecraft including the Solar Anomalous and Magnetospheric Particle Explorer (SAMPEX) (e.g. Blake et al., 1996; Blum et al., 2015; Douma et al., 2019, 2017; Greeley et al., 2019; Lorentzen et al., 2001a,b; Nakamura et al., 1995, 2000; O'Brien et al., 2004, 2003), Montana State University's (MSU) Focused Investigation

344 of Relativistic Electron Bursts: Intensity, Range, and Dynamics II (FIREBIRD-II)  
 345 (Anderson et al., 2017; Breneman et al., 2017; Crew et al., 2016; Klumpar et al.,  
 346 2015; Spence et al., 2012), and Science Technologies Satellite (STSAT-I) (e.g. Lee  
 347 et al., 2012, 2005). An example microburst time series is shown in Fig. 1.12 and was  
 348 observed by the FIREBIRD-II CubeSats. The prominent features of the example  
 349 microbursts in Fig. 1.12 are their sub-second duration, half order of magnitude  
 350 increase in count rate above the falling background, and their 200-800 keV energy  
 351 extent.

352 Microbursts are observed on magnetic field footprints that are connected to the  
 353 outer radiation belt (approximately  $4 < L < 8$ ). They are predominately observed in  
 354 the 0-12 MLT sector with an elevated occurrence frequency during magnetospherically  
 355 disturbed times as shown in Fig. 1.13 (e.g. Douma et al., 2017). O'Brien et al. (2003)  
 356 used SAMPEX relativistic electron data and found that microbursts predominately  
 357 occur during the main phase of storms, with a heightened occurrence rate during the  
 358 recovery phase. Microburst occurrence rates are also higher during high solar wind  
 359 velocity events e.g. from co-rotating interaction regions (Greeley et al., 2019; O'Brien  
 360 et al., 2003).

361 The estimated impact of microbursts on the atmosphere and the radiation  
 362 belts is significant. Relativistic microburst electrons impacting the atmosphere are  
 363 ionized at  $< 100$  km altitudes, with higher energy electrons penetrating closer to  
 364 the surface. The resulting chemical reaction of microburst electrons impacting the  
 365 atmosphere produces odd hydrogen  $\text{HO}_x$  and odd nitrogen  $\text{NO}_x$  molecules, which  
 366 are partially responsible for destroying ozone ( $\text{O}_3$ ). Seppälä et al. (2018) modeled  
 367 a six hour relativistic microburst storm and found that the mesospheric ozone was  
 368 reduced by 7 – 12% in the summer months and 12 – 20% in the winter months, so  
 369 microbursts may have a non-negligible contribution to the dynamics of atmospheric

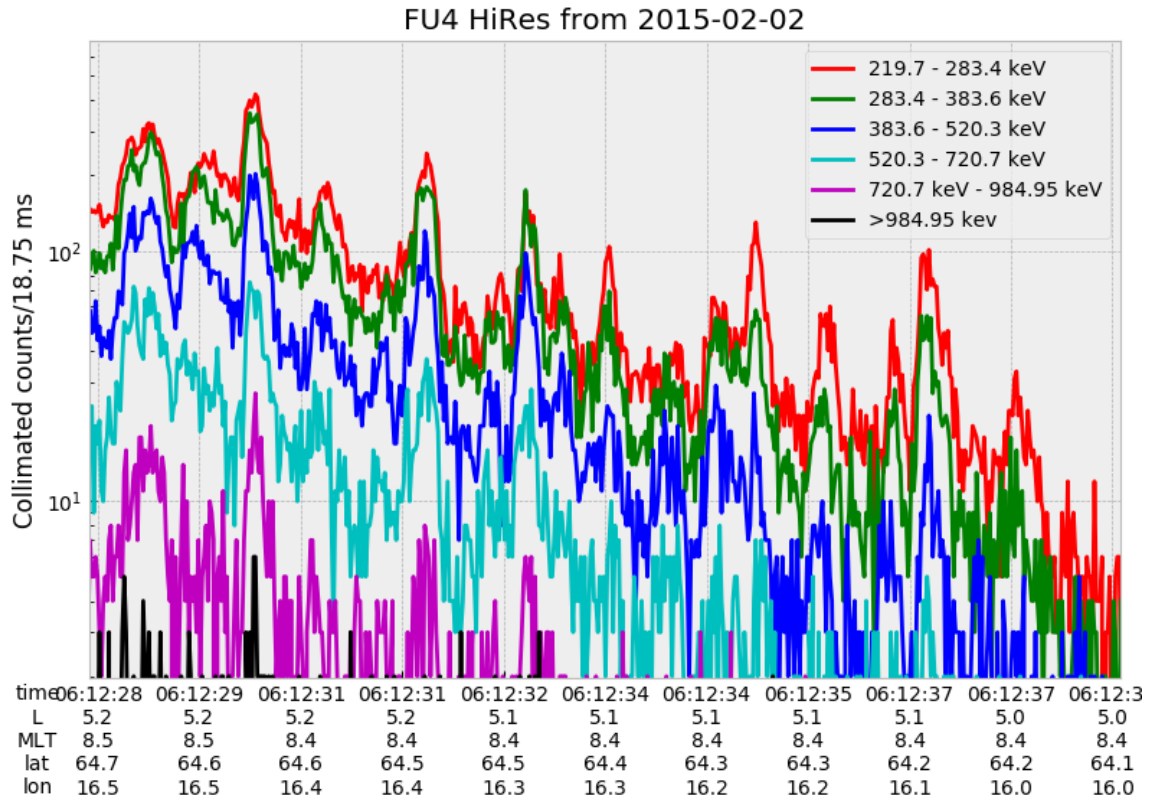


Figure 1.12: An example train of microbursts observed by FIREBIRD-II unit 4 on February 2nd, 2015. The colored curves show the differential energy channel count rates in five channels from  $\approx 200$  keV to 1 MeV and a sixth integral energy channel with a 1 MeV threshold. The x-axis labels show auxiliary information such as time of observation and the spacecraft position in L, MLT, latitude and longitude coordinates.

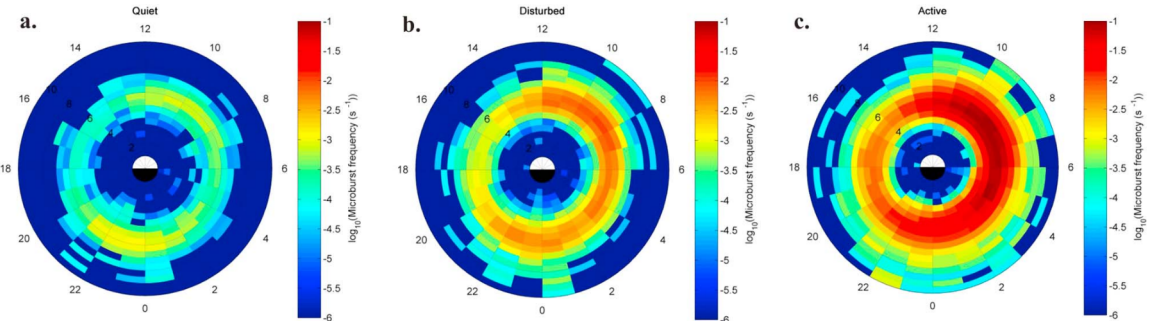


Figure 1.13: Distribution of  $> 1$  MeV microburst occurrence rates as a function of L and MLT. The three panels show the microburst occurrence rate dependence on geomagnetic activity, parameterized by the auroral electrojet (AE) index for (a)  $\text{AE} < 100 \text{ nT}$ , (b)  $100 < \text{AE} < 300 \text{ nT}$  and (c)  $\text{AE} > 300 \text{ nT}$ . Figure from Douma et al. (2017).

ozone. Furthermore, microbursts have also been estimated to have a significant impact on the outer radiation belt electron population. Radiation belt electron loss due to microbursts has been estimated to be on the order of a day (Breneman et al., 2017; Douma et al., 2019; Lorentzen et al., 2001b; O'Brien et al., 2004; Thorne et al., 2005).

The wave-particle interactions responsible for generating microbursts are also believed to accelerate electrons in the radiation belts. As mentioned earlier, when an electron is in resonance with a wave, energy is exchanged with the wave and the electron is either accelerated or decelerated. The signature of wave-particle acceleration been observed for radiation belt electrons (e.g. Horne et al., 2005; Meredith et al., 2002; Reeves et al., 2013), and O'Brien et al. (2003) presented evidence that enhancements in chorus waves, microbursts, and radiation belt electrons are related. To explain their observations, O'Brien et al. (2003) proposed that microburst precipitation is a side effect of electron acceleration due to chorus waves.

The widely used theoretical framework to model the wave-particle interactions responsible for accelerating electrons and scattering microbursts is quasi-linear

386 diffusion (e.g. Horne et al., 2005; Meredith et al., 2002; Summers, 2005; Summers  
 387 et al., 1998; Thorne et al., 2005; Walker, 1993). This framework is explained in  
 388 Chapter ??, and applied to an observation of a microburst in the heart of the  
 389 radiation belt. Qualitatively, when a particle is resonant with a wave it can either  
 390 be transported in pitch angle towards the loss cone and lose energy to the wave, or  
 391 transported away from the loss cone and gain energy from the wave.

392 As previously mentioned, the range of observed microburst energies range from a  
 393 few tens of keV (e.g Datta et al., 1997; Parks, 1967) to greater than 1 MeV (e.g. Blake  
 394 et al., 1996; Greeley et al., 2019). The microburst electron flux ( $J$ ) falls off in energy,  
 395 and the microburst energy spectra is typically well fit to a decaying exponential

$$J(E) = J_0 e^{-E/E_0} \quad (1.22)$$

396 where  $J_0$  is the flux at 0 keV (unphysical free parameter) and  $E_0$  quantifies the  
 397 efficiency of the scattering mechanism in energy (e.g. Datta et al., 1997; Lee et al.,  
 398 2005; Parks, 1967). A small  $E_0$  suggests that mostly low energy particles are scattered.  
 399 In contrast a high  $E_0$  suggests that the scattering mechanism scatters low and high  
 400 energy electrons. Reality is a bit more messy and a high  $E_0$  may be a signature of  
 401 a scattering mechanism preferential to high energy electrons, but is hidden by the  
 402 convolution of the source particles available to be scattered (typically with a falling  
 403 energy spectrum) and the energy-dependent efficiency of the scattering mechanism.

404 The short microburst duration observed by a single LEO satellite has an  
 405 ambiguity when interpreting what is exactly a microburst. The two possible realities  
 406 are: a microburst is very small and spatially stationary so that the LEO spacecraft  
 407 passes through it in less than a second. Alternatively, microbursts are spatially large  
 408 and transient so a microburst will pass by the spacecraft in a fraction of a second.

<sup>409</sup> There are a few ways to distinguish between the two possible realities, and each one  
<sup>410</sup> has a unique set of advantages.

<sup>411</sup> A high altitude balloon provides essentially a stationary view of the precipitating  
<sup>412</sup> particles under the radiation belt footprints. A short-lived, temporal microburst can  
<sup>413</sup> be unambiguously identified. Spatial structures, on the other hand, are difficult to  
<sup>414</sup> identify because a balloon is essentially still on drift timescales.

<sup>415</sup> Multi-spacecraft missions are an alternate solution that can determine if a  
<sup>416</sup> microburst is spatial or temporal. As will be shown in this dissertation, if a microburst  
<sup>417</sup> is observed simultaneously by two spacecraft then it is temporal and has a size  
<sup>418</sup> greater than the spacecraft separation. On the contrary, if two spacecraft observe  
<sup>419</sup> a microburst-like feature at different times but at the same location, then the feature  
<sup>420</sup> is spatial and may be a curtain (Blake and O'Brien, 2016). Both balloon and multi-  
<sup>421</sup> spacecraft observational methods have a unique set of strengths, and this dissertation  
<sup>422</sup> takes the multi-spacecraft approach to identify and study microbursts.

<sup>423</sup> Scope of Reserach

<sup>424</sup> This dissertation furthers our understanding of the microburst scattering  
<sup>425</sup> mechanism by presenting observational evidence of microburst scattering directly, and  
<sup>426</sup> measuring microburst sizes and comparing them to the size of chorus waves. Chapter  
<sup>427</sup> ?? describes a microburst scattering event observed by NASA's Van Allen Probes.  
<sup>428</sup> For this event, particle and wave measurements were analyzed and modeled in the  
<sup>429</sup> theoretical framework of pitch angle and energy diffusion. Then the following two  
<sup>430</sup> chapters present studies of microburst sizes in comparison to chorus waves. Chapter  
<sup>431</sup> ?? describes a bouncing packet microburst observation made by the FIREBIRD-II  
<sup>432</sup> mission where the microburst's lower bound longitudinal and latitudinal sizes were  
<sup>433</sup> estimated. Then Chapter ?? expands the case study from Chapter ?? to a statistical

434 study of microburst sizes using The Aerospace Corporation’s AeroCube-6 (AC6)  
435 CubeSats. In this study, a Monte Carlo and analytic microburst size models were  
436 developed to account for the compounding statistical effects of random microburst  
437 sizes and locations. Lastly, Chapter ?? will summarize this work and make concluding  
438 remarks regarding outstanding questions in microburst physics.

## Bibliography

- 439
- 440 Anderson, B., Shekhar, S., Millan, R., Crew, A., Spence, H., Klumpar, D., Blake, J.,  
441 O'Brien, T., and Turner, D. (2017). Spatial scale and duration of one microburst  
442 region on 13 August 2015. *Journal of Geophysical Research: Space Physics*.
- 443 Anderson, K. A. and Milton, D. W. (1964). Balloon observations of X rays in the  
444 auroral zone: 3. High time resolution studies. *Journal of Geophysical Research*,  
445 69(21):4457–4479.
- 446 Barcus, J., Brown, R., and Rosenberg, T. (1966). Spatial and temporal character of  
447 fast variations in auroral-zone x rays. *Journal of Geophysical Research*, 71(1):125–  
448 141.
- 449 Baumjohann, W. and Treumann, R. A. (1997). *Basic space plasma physics*. World  
450 Scientific.
- 451 Blake, J.,Looper, M., Baker, D., Nakamura, R., Klecker, B., and Hovestadt, D.  
452 (1996). New high temporal and spatial resolution measurements by sampex of the  
453 precipitation of relativistic electrons. *Advances in Space Research*, 18(8):171 – 186.
- 454 Blake, J. B. and O'Brien, T. P. (2016). Observations of small-scale latitudinal  
455 structure in energetic electron precipitation. *Journal of Geophysical Research: Space  
456 Physics*, 121(4):3031–3035. 2015JA021815.
- 457 Blum, L., Li, X., and Denton, M. (2015). Rapid MeV electron precipitation as  
458 observed by SAMPEX/HILT during high-speed stream-driven storms. *Journal of  
459 Geophysical Research: Space Physics*, 120(5):3783–3794. 2014JA020633.
- 460 Breneman, A., Crew, A., Sample, J., Klumpar, D., Johnson, A., Agapitov, O.,  
461 Shumko, M., Turner, D., Santolik, O., Wygant, J., et al. (2017). Observations  
462 directly linking relativistic electron microbursts to whistler mode chorus: Van allen  
463 probes and FIREBIRD II. *Geophysical Research Letters*.
- 464 Breneman, A. W., Halford, A., Millan, R., McCarthy, M., Fennell, J., Sample, J.,  
465 Woodger, L., Hospodarsky, G., Wygant, J. R., Cattell, C. A., et al. (2015). Global-  
466 scale coherence modulation of radiation-belt electron loss from plasmaspheric hiss.  
467 *Nature*, 523(7559):193.
- 468 Brown, R., Barcus, J., and Parsons, N. (1965). Balloon observations of auroral zone  
469 x rays in conjugate regions. 2. microbursts and pulsations. *Journal of Geophysical  
470 Research (U.S.)*.
- 471 Capannolo, L., Li, W., Ma, Q., Shen, X.-C., Zhang, X.-J., Redmon, R., Rodriguez,  
472 J., Engebretson, M., Kletzing, C., Kurth, W., et al. (2019). Energetic electron  
473 precipitation: multi-event analysis of its spatial extent during emic wave activity.  
474 *Journal of Geophysical Research: Space Physics*.

- 475 Claudepierre, S., O'Brien, T.,Looper, M., Blake, J., Fennell, J., Roeder, J.,  
 476 Clemmons, J., Mazur, J., Turner, D., Reeves, G., et al. (2019). A revised look  
 477 at relativistic electrons in the earth's inner radiation zone and slot region. *Journal*  
 478 *of Geophysical Research: Space Physics*, 124(2):934–951.
- 479 Crew, A. B., Spence, H. E., Blake, J. B., Klumpar, D. M., Larsen, B. A., O'Brien,  
 480 T. P., Driscoll, S., Handley, M., Legere, J., Longworth, S., Mashburn, K.,  
 481 Mosleh, E., Ryhajlo, N., Smith, S., Springer, L., and Widholm, M. (2016). First  
 482 multipoint in situ observations of electron microbursts: Initial results from the  
 483 NSF FIREBIRD II mission. *Journal of Geophysical Research: Space Physics*,  
 484 121(6):5272–5283. 2016JA022485.
- 485 Datta, S., Skoug, R., McCarthy, M., and Parks, G. (1997). Modeling of microburst  
 486 electron precipitation using pitch angle diffusion theory. *Journal of Geophysical*  
 487 *Research: Space Physics*, 102(A8):17325–17333.
- 488 Douma, E., Rodger, C., Blum, L., O'Brien, T., Clilverd, M., and Blake, J. (2019).  
 489 Characteristics of relativistic microburst intensity from sampex observations.  
 490 *Journal of Geophysical Research: Space Physics*.
- 491 Douma, E., Rodger, C. J., Blum, L. W., and Clilverd, M. A. (2017). Occurrence  
 492 characteristics of relativistic electron microbursts from SAMPEX observations.  
 493 *Journal of Geophysical Research: Space Physics*, 122(8):8096–8107. 2017JA024067.
- 494 Eastwood, J., Hietala, H., Toth, G., Phan, T., and Fujimoto, M. (2015). What  
 495 controls the structure and dynamics of earths magnetosphere? *Space Science*  
 496 *Reviews*, 188(1-4):251–286.
- 497 Fang, X., Randall, C. E., Lummerzheim, D., Wang, W., Lu, G., Solomon, S. C., and  
 498 Frahm, R. A. (2010). Parameterization of monoenergetic electron impact ionization.  
 499 *Geophysical Research Letters*, 37(22).
- 500 Greeley, A., Kanekal, S., Baker, D., Klecker, B., and Schiller, Q. (2019). Quantifying  
 501 the contribution of microbursts to global electron loss in the radiation belts. *Journal*  
 502 *of Geophysical Research: Space Physics*.
- 503 Hendry, A. T., Rodger, C. J., and Clilverd, M. A. (2017). Evidence of sub-mev  
 504 emic-driven electron precipitation. *Geophysical Research Letters*, 44(3):1210–1218.
- 505 Horne, R., Glauert, S., Meredith, N., Boscher, D., Maget, V., Heynderickx, D., and  
 506 Pitchford, D. (2013). Space weather impacts on satellites and forecasting the earth's  
 507 electron radiation belts with spacecast. *Space Weather*, 11(4):169–186.
- 508 Horne, R., Glauert, S., and Thorne, R. (2003). Resonant diffusion of radiation belt  
 509 electrons by whistler-mode chorus. *Geophysical research letters*, 30(9).

- 510 Horne, R. B., Thorne, R. M., Shprits, Y. Y., Meredith, N. P., Glauert, S. A., Smith,  
 511 A. J., Kanekal, S. G., Baker, D. N., Engebretson, M. J., Posch, J. L., et al.  
 512 (2005). Wave acceleration of electrons in the van allen radiation belts. *Nature*,  
 513 437(7056):227.
- 514 Kasahara, S., Miyoshi, Y., Yokota, S., Mitani, T., Kasahara, Y., Matsuda, S.,  
 515 Kumamoto, A., Matsuoka, A., Kazama, Y., Frey, H., et al. (2018). Pulsating  
 516 aurora from electron scattering by chorus waves. *Nature*, 554(7692):337.
- 517 Klumpar, D., Springer, L., Mosleh, E., Mashburn, K., Berardinelli, S., Gunderson,  
 518 A., Handly, M., Ryhajlo, N., Spence, H., Smith, S., Legere, J., Widholm, M.,  
 519 Longworth, S., Crew, A., Larsen, B., Blake, J., and Walmsley, N. (2015). Flight  
 520 system technologies enabling the twin-cubesat firebird-ii scientific mission.
- 521 Lee, J. J., Parks, G. K., Lee, E., Tsurutani, B. T., Hwang, J., Cho, K. S., Kim, K.-H.,  
 522 Park, Y. D., Min, K. W., and McCarthy, M. P. (2012). Anisotropic pitch angle  
 523 distribution of 100 keV microburst electrons in the loss cone: measurements from  
 524 STSAT-1. *Annales Geophysicae*, 30(11):1567–1573.
- 525 Lee, J.-J., Parks, G. K., Min, K. W., Kim, H. J., Park, J., Hwang, J., McCarthy,  
 526 M. P., Lee, E., Ryu, K. S., Lim, J. T., Sim, E. S., Lee, H. W., Kang, K. I., and  
 527 Park, H. Y. (2005). Energy spectra of 170–360 keV electron microbursts measured  
 528 by the korean STSAT-1. *Geophysical Research Letters*, 32(13). L13106.
- 529 Li, X., Selesnick, R., Schiller, Q., Zhang, K., Zhao, H., Baker, D. N., and Temerin,  
 530 M. A. (2017). Measurement of electrons from albedo neutron decay and neutron  
 531 density in near-earth space. *Nature*, 552(7685):382.
- 532 Lorentzen, K. R., Blake, J. B., Inan, U. S., and Bortnik, J. (2001a). Observations  
 533 of relativistic electron microbursts in association with VLF chorus. *Journal of  
 534 Geophysical Research: Space Physics*, 106(A4):6017–6027.
- 535 Lorentzen, K. R.,Looper, M. D., and Blake, J. B. (2001b). Relativistic electron  
 536 microbursts during the GEM storms. *Geophysical Research Letters*, 28(13):2573–  
 537 2576.
- 538 Lyons, L. R. and Thorne, R. M. (1973). Equilibrium structure of radiation belt  
 539 electrons. *Journal of Geophysical Research*, 78(13):2142–2149.
- 540 Meredith, N., Horne, R., Summers, D., Thorne, R., Iles, R., Heynderickx, D., and  
 541 Anderson, R. (2002). Evidence for acceleration of outer zone electrons to relativistic  
 542 energies by whistler mode chorus. In *Annales Geophysicae*, volume 20, pages 967–  
 543 979.
- 544 Millan, R. and Thorne, R. (2007). Review of radiation belt relativistic electron losses.  
 545 *Journal of Atmospheric and Solar-Terrestrial Physics*, 69(3):362 – 377.

- 546 Nakamura, R., Baker, D. N., Blake, J. B., Kanekal, S., Klecker, B., and Hovestadt,  
 547 D. (1995). Relativistic electron precipitation enhancements near the outer edge of  
 548 the radiation belt. *Geophysical Research Letters*, 22(9):1129–1132.
- 549 Nakamura, R., Isowa, M., Kamide, Y., Baker, D., Blake, J., and Looper, M. (2000).  
 550 Observations of relativistic electron microbursts in association with VLF chorus.  
 551 *J. Geophys. Res.*, 105:15875–15885.
- 552 O'Brien, T., Claudepierre, S., Blake, J., Fennell, J. F., Clemons, J., Roeder, J.,  
 553 Spence, H. E., Reeves, G., and Baker, D. (2014). An empirically observed pitch-  
 554 angle diffusion eigenmode in the earth's electron belt near  $l^*= 5.0$ . *Geophysical*  
 555 *Research Letters*, 41(2):251–258.
- 556 O'Brien, T., Claudepierre, S., Guild, T., Fennell, J., Turner, D., Blake, J., Clemons,  
 557 J., and Roeder, J. (2016). Inner zone and slot electron radial diffusion revisited.  
 558 *Geophysical Research Letters*, 43(14):7301–7310.
- 559 O'Brien, T. and Moldwin, M. (2003). Empirical plasmapause models from magnetic  
 560 indices. *Geophysical Research Letters*, 30(4).
- 561 O'Brien, T. P., Looper, M. D., and Blake, J. B. (2004). Quantification of relativistic  
 562 electron microburst losses during the GEM storms. *Geophysical Research Letters*,  
 563 31(4). L04802.
- 564 O'Brien, T. P., Lorentzen, K. R., Mann, I. R., Meredith, N. P., Blake, J. B., Fennell,  
 565 J. F., Looper, M. D., Milling, D. K., and Anderson, R. R. (2003). Energization of  
 566 relativistic electrons in the presence of ULF power and MeV microbursts: Evidence  
 567 for dual ULF and VLF acceleration. *Journal of Geophysical Research: Space*  
 568 *Physics*, 108(A8).
- 569 Ozaki, M., Miyoshi, Y., Shiokawa, K., Hosokawa, K., Oyama, S.-i., Kataoka, R.,  
 570 Ebihara, Y., Ogawa, Y., Kasahara, Y., Yagitani, S., et al. (2019). Visualization of  
 571 rapid electron precipitation via chorus element wave–particle interactions. *Nature*  
 572 *communications*, 10(1):257.
- 573 Parks, G. K. (1967). Spatial characteristics of auroral-zone X-ray microbursts. *Journal*  
 574 *of Geophysical Research*, 72(1):215–226.
- 575 Reeves, G., Spence, H. E., Henderson, M., Morley, S., Friedel, R., Funsten, H., Baker,  
 576 D., Kanekal, S., Blake, J., Fennell, J., et al. (2013). Electron acceleration in the  
 577 heart of the van allen radiation belts. *Science*, 341(6149):991–994.
- 578 Reeves, G. D., McAdams, K. L., Friedel, R. H. W., and O'Brien, T. P. (2003). Ac-  
 579 celeration and loss of relativistic electrons during geomagnetic storms. *Geophysical*  
 580 *Research Letters*, 30(10):n/a–n/a. 1529.

- 581 Schulz, M. and Lanzerotti, L. J. (1974). *Particle Diffusion in the Radiation Belts*.  
 582 Springer.
- 583 Seppälä, A., Douma, E., Rodger, C., Verronen, P., Clilverd, M. A., and Bortnik, J.  
 584 (2018). Relativistic electron microburst events: Modeling the atmospheric impact.  
 585 *Geophysical Research Letters*, 45(2):1141–1147.
- 586 Spence, H. E., Blake, J. B., Crew, A. B., Driscoll, S., Klumpar, D. M., Larsen,  
 587 B. A., Legere, J., Longworth, S., Mosleh, E., O'Brien, T. P., Smith, S., Springer,  
 588 L., and Widholm, M. (2012). Focusing on size and energy dependence of electron  
 589 microbursts from the van allen radiation belts. *Space Weather*, 10(11).
- 590 Summers, D. (2005). Quasi-linear diffusion coefficients for field-aligned electro-  
 591 magnetic waves with applications to the magnetosphere. *Journal of Geophysical  
 592 Research: Space Physics*, 110(A8):n/a–n/a. A08213.
- 593 Summers, D., Thorne, R. M., and Xiao, F. (1998). Relativistic theory of wave-particle  
 594 resonant diffusion with application to electron acceleration in the magnetosphere.  
 595 *Journal of Geophysical Research: Space Physics*, 103(A9):20487–20500.
- 596 Thorne, R. M., O'Brien, T. P., Shprits, Y. Y., Summers, D., and Horne, R. B. (2005).  
 597 Timescale for MeV electron microburst loss during geomagnetic storms. *Journal  
 598 of Geophysical Research: Space Physics*, 110(A9). A09202.
- 599 Trefall, H., Bjordal, J., Ullaland, S., and Stadsnes, J. (1966). On the extension of  
 600 auroral-zone x-ray microbursts. *Journal of Atmospheric and Terrestrial Physics*,  
 601 28(2):225–233.
- 602 Tsurutani, B. T. and Lakhina, G. S. (1997). Some basic concepts of wave-particle  
 603 interactions in collisionless plasmas. *Reviews of Geophysics*, 35(4):491–501.
- 604 Ukhorskiy, A. Y., Anderson, B. J., Brandt, P. C., and Tsyganenko, N. A. (2006).  
 605 Storm time evolution of the outer radiation belt: Transport and losses. *Journal of  
 606 Geophysical Research: Space Physics*, 111(A11):n/a–n/a. A11S03.
- 607 Van Allen, J. A. (1959). The geomagnetically trapped corpuscular radiation. *Journal  
 608 of Geophysical Research*, 64(11):1683–1689.
- 609 Vernov, S. and Chudakov, A. (1960). Investigation of radiation in outer space. In  
 610 *International Cosmic Ray Conference*, volume 3, page 19.
- 611 Walker, A. D. M. (1993). *Plasma waves in the magnetosphere*, volume 24. Springer  
 612 Science & Business Media.